Metal Amorphous Nanocomposite (MANC) Alloy Cores with Spatially Tuned Permeability for Advanced Power Magnetics Applications

K. BYERLY,[1,2,8] P.R. OHODNICKI,[1] S.R. MOON,[1,3] A.M. LEARY,[4] V. KEYLIN,[4,5] M.E. MCHENRY,[6] S. SIMIZU,[6] R. BEDDINGFIELD,[7] Y. YU,[1,2] G. FEICHTER,[4,5] R. NOEBE,[4] R. BOWMAN,[4] and S. BHATTACHARYA[7]

1.—National Energy Technology Laboratory, Pittsburgh, PA, USA. 2.—AECOM, Contractor to the US Department of Energy, Pittsburgh, PA, USA. 3.—Oak Ridge Institute for Science and Education, US Department of Energy, Oak Ridge, TN, USA. 4.—Materials and Structures Division, NASA Glenn Research Center, Cleveland, OH, USA. 5.—Vantage Partners LLC, Brook Park, OH, USA. 6.—Materials Science and Engineering, Carnegie Mellon University, Pittsburgh, PA, USA. 7.—North Carolina State University, Raleigh, NC, USA. 8.—e-mail: kevin.byerly@netl.doe.gov

Metal amorphous nanocomposite (MANC) alloys are an emerging class of soft magnetic materials showing promise for a range of inductive components targeted for higher power density and higher efficiency power conversion applications including inductors, transformers, and rotating electrical machinery. Magnetization reversal mechanisms within these alloys are typically determined by composition optimization as well as controlled annealing treatments to generate a nanocomposite structure composed of nanocrystals embedded in an amorphous precursor. Here we demonstrate the concept of spatially varying the permeability within a given component for optimization of performance by using the strain annealing process. The concept is realized experimentally through the smoothing of the flux profile from the inner to outer core radius achieved by a monotonic variation in tension during the strain annealing process. Great potential exists for an extension of this concept to a wide range of other power magnetic components and more complex spatially varying permeability profiles through advances in strain annealing techniques and controls.

INTRODUCTION

Advanced power magnetic components are seeing renewed interest in recent years because of a number of evolving societal trends. First, the electrical transmission and distribution system is aging and outdated as it was originally designed for a paradigm in which large centralized generation systems delivered one-way power to the transmission lines and eventually the distribution systems. With increasing penetration of renewables and other distributed generation resources (solar photovoltaic, wind, fuel cells, microturbines, etc.), a transformation is underway to an electrical power system capable of multi-directional power flow, demand response, and microgrid operation to ensure reliable and secure electrical power delivery in a more complex, distributed system. Grid resiliency and reliability would also be enhanced through replacement of large power transformers with more modular, solid-state transformers. Paramount to the successful realization of this vision will be advances in grid-tied inverters, power flow controllers, solid-state transformers, and sensors based upon advanced soft magnetic materials (SMMs) and components that can operate at unprecedented combinations of frequencies, power ratings, and efficiencies. These needs are made even more acute because of the opportunities and challenges to magnetic components driven by recent advances in wide bandgap semiconductor switching devices based upon SiC, GaN, and others. Second, electrical machinery accounts for a large fraction of industrial energy utilization within the US domestic economy, and increased efficiencies of motors and generators can have a significant impact on overall energy efficiency. Advances in drives as well as the magnetic materials comprising the stator and rotor, particularly for rare earth-free solutions, are increasingly important moving into the future. Third, the trend toward electrification of the transportation fleet spanning automotive/trucking, aviation, aerospace, rail, and naval systems is driving a need for power electronics converters and motors that can operate at temperatures and efficiencies with higher power densities than previously demanded. In such applications, the enabling magnetic materials and components will play a key role in the successful realization of efficient, reliable, and power-dense solutions to satisfy increasingly stringent technologic needs.

Metal amorphous nanocomposite (MANC) alloys are an emerging class of soft magnetic materials for a number of applications spanning power electronics, transformers, and rotating electrical machinery. Interest in MANC SMMs derives from the synergy in properties of the amorphous and crystalline phases from which they are composed. These materials have been termed *nanocrystalline* materials as commercial products, such as FINEMET®; however, their superior properties derive from the distinct properties of both the amorphous and nanocrystalline phases, and therefore the term *nanocomposite* is more accurate.[1,2] The first step in producing this class of alloys is through rapid solidification processing techniques to form long amorphous metal ribbons (AMRs) approximately 13–25 microns in thickness, millimeters to 100 s of millimeters in width, and meters to kilometers in length. Synthesized AMRs are then subjected to optimized annealing treatments to generate a MANC structure composed of nanocrystals embedded within an amorphous precursor.[1,2] For conventional manufacturing processes of this class of alloys, there are many challenges: (1) the majority of MANC alloys become brittle during annealing treatments, which makes subsequent handling prohibitively difficult from a manufacturing perspective, (2) many annealing treatments require careful control of time and temperature, which is challenging for fully wound fabricated cores, and (3) with post-processing, such as impregnation and gapping, degradation of both physical and magnetic properties results from the magnetoelastic coupling stresses introduced during the resin curing and the subsequent cutting process.

In-line processes, however, can be extremely valuable in terms of additional flexibility of alloy and material property optimization as well as enhanced control of localized properties in the core by application of time-varying mechanical, magnetic, or other applied fields that impact the ultimate material performance. By using a compatible alloy that permits in-line annealing treatments before winding into the final geometry, most of these challenges and side effects can be eliminated, thus allowing for a range of options for optimizing properties and performance at the core level. MANC alloy systems can exhibit transverse[3–5] or longitudinal[6] induced magnetic anisotropy. Of the available MANC systems, the Co-Fe-Nb-Si-B based alloys have shown clearly superior mechanical properties and ductility in addition to significantly enhanced responses to strain annealing techniques compared with commercially available Fe-based alloys, making them excellent candidates for demonstration of the potential for advanced in-line processing methods and techniques.[4,5] Their transverse induced anisotropy is tunable over nearly five orders of magnitude, enabling certain power inductor applications.

A plot of the relative strain-induced anisotropy is demonstrated in Fig. 1a for a number of Co-based MANC alloys compared with traditional iron-based alloys such as $Fe_{73.5}Nb_3Si_{15.5}B_7Cu_1$.[3–5,7] As can be clearly observed, the Co-based alloys show a figure of merit of induced anisotropy per unit applied tensile

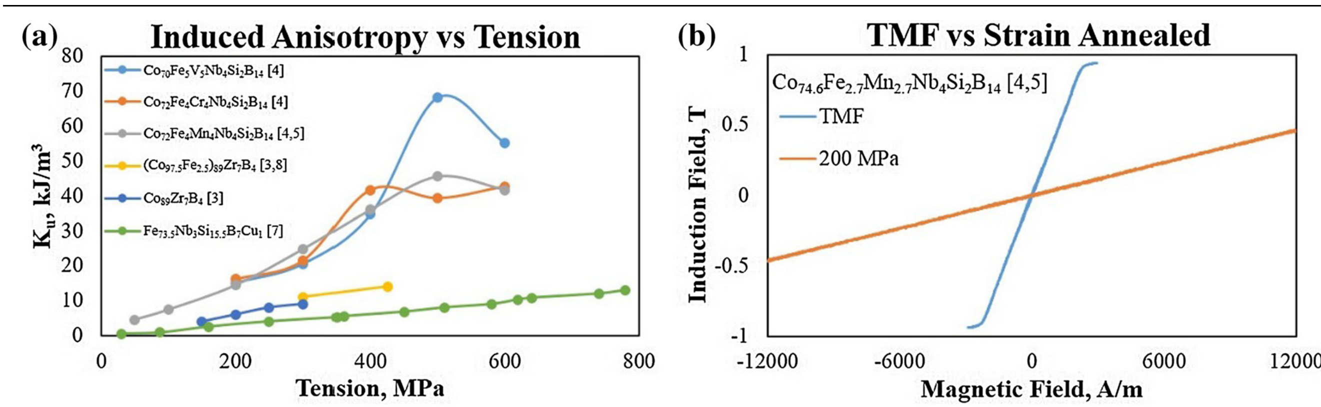

Fig. 1. (a) Graphical comparison of strain-induced anisotropy that forms during crystallization for amorphous/nanocrystalline soft magnetic alloys showing the largest responses obtained for Co-rich alloys. (b) Plot of quasistatic *B-H* loops for TMF-induced anisotropy compared with strain-induced anisotropy for a representative Co-rich alloy.

stress of $\sim$ 2–10× that of the Fe-based alloys. In addition, the Co-based MANC alloys have significantly improved mechanical properties so that scalable manufacturing processes can be successfully implemented at much higher applied tensions than for corresponding Fe-based alloys.[8] Figure 1b further emphasizes that the response to strain annealing is much greater than that of traditional transverse magnetic field (TMF) annealing techniques. A significantly greater applied field is necessary to saturate the magnetization of the strain annealed material compared with TMF-annealed material. As a result, the demonstrated anisotropy fields obtainable through strain annealing are roughly ten times those through TMF annealing ($\sim$ 10–40 Oe through field annealing[9,10] and $\sim$ 100–400 Oe through strain annealing[3]).

One of the MANC alloy systems of particular interest for in-line annealing treatments, such as strain annealing, includes compositions in the range of $Co_{80\text{-}x\text{-}y}Fe_xMn_yNb_4Si_2B_{14}$[4] with x and y that can be chosen specifically to achieve a range of permeabilities from as low as $\sim$ 10 to as high as $\sim$ 10,000. These alloys exhibit a relatively high strain-induced anisotropy with dramatically improved mechanical properties to permit successful manufacturing-scale strain annealing and subsequent ribbon handling for core fabrication purposes. Many component and system level advantages can be realized through optimization of the permeability of a core or power magnetic component. For example, through controllably tuning permeability of the Co-based MANC alloy systems through in-line strain annealing in a spatially uniform manner, the need for gapping of inductor cores can be potentially eliminated, yielding significant component level advantages such as reduced EMI and losses surrounding the air gaps. By exploiting the potential to vary the applied tension as a function of ribbon length,[11] a spatially varying permeability can be accomplished that can yield important benefits such as smoothing flux distributions throughout a power magnetic component to minimize peak temperature rise and, in some cases, reduce overall losses. A key example of such an approach is to grade an inductor core permeability from the inner to outer radius such that the flux concentration at the inner radius and the associated peak in losses and temperature rise can be reduced and mitigated. We focus on this specific application in this manuscript as a proof-of-concept demonstration for this paradigm shift in the engineering of soft magnetic cores and components for power magnetic applications.

EXPERIMENTAL PROCEDURE

Alloy Synthesis and Strain Annealing

Co-based AMR ($Co_{74.6}Fe_{2.7}Mn_{2.7}Nb_4Si_2B_{14}$), approximately 25 mm wide, was produced through planar flow casting (PFC) in air using a pilot-scale custom-designed planar flow casting system. The AMR was then spooled and subjected to a controlled strain annealing process under a regulated value of applied tension. This process partially devitrifies the material, resulting in a magnetically anisotropic nanocomposite structure (amorphous matrix containing nanocrystalline grains). A schematic and setup picture of the overall strain annealing system is presented in Fig. 2. The strain annealing system is laced from the unwind spool to the rewind spool starting from the stock ribbon unwind spool of 25 mm wide, $\sim$ 20 μm thick continuous ribbon (700 m in length). The process is continuous and automated. The ribbon is passed through a thermal heating zone while tension is applied along the ribbon axis. The anneal tension is maintained between the unwind spool and rubber-coated drive rollers, and the control of this tension as a function of length enables permeability tuning in a uniformly or spatially varying manner along the ribbon.

Through appropriate control of the strain annealing system, three different tension profiles are achievable to allow for (1) tunable, (2) graded, and (3) cyclic ribbon permeability variation. With each tension profile, the unwind tension is controlled as a function of length. Other strain annealing machine processing conditions, such as material speed/time in furnace, anneal temperature, and rewind tension, are held constant during the experiments.

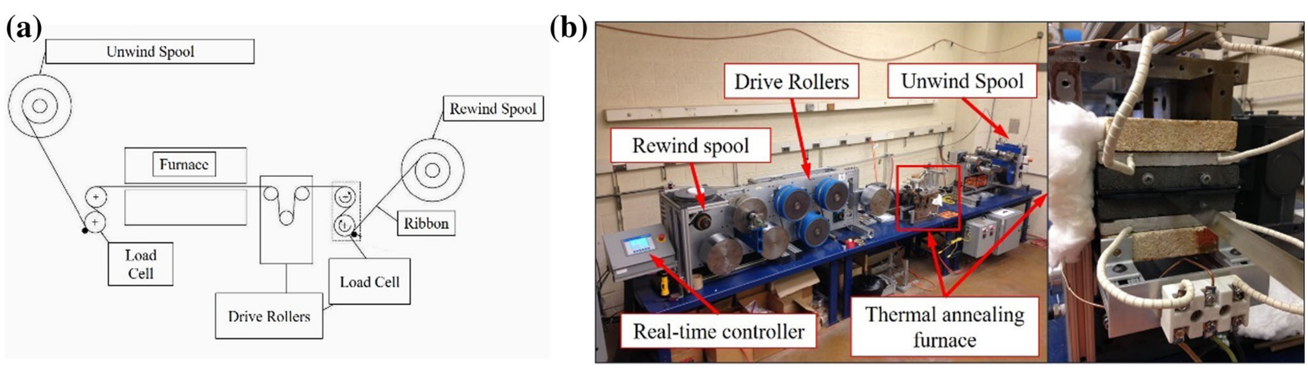

Fig. 2. (a) Schematic illustration of a strain annealing system. (b) Pilot-scale strain anneal system setup with enlarged view of the furnace.

Magnetic Property Measurements (Core Losses and Permeability)

The core loss measurements are based on measured B-H loop characteristics,[12] and the conceptual configuration for such measurements is shown in Fig. 3. A primary (excitation) winding and secondary (sense) winding are placed around the device under test (DUT). The magnetic field strength H is proportional to the primary current i in the excitation winding as

$$H(t) = \frac{N_1 \cdot i(t)}{l_e} \tag{1}$$

where N_1 is the number of the excitation winding turns, and l_e is the effective magnetic path length of the DUT. The flux density B is proportional to the integral of the sense winding voltage v as

$$B(t) = \frac{1}{N_2 \cdot A_e} \int_0^T v(\tau) d\tau \tag{2}$$

where N_2 is the number of sense winding turns, A_e is the effective core cross section of the DUT, and T is period of the excitation voltage. The core losses are equivalent to the enclosed area of the B-H loop multiplied by the frequency f. The core losses are normalized by per unit weight as

$$P/W = f \oint H \mathrm{d}B \tag{3}$$

where P is the measured core losses, and W is the core weight. The permeability is measured using the peak values of B and H as

$$\mu = \mu_r \cdot \mu_o = B_{\text{peak}}/H_{\text{peak}} \tag{4}$$

Using this method, only measurements of the primary current i and the secondary voltage v are required. The primary current i is measured using a Keysight N2893A current probe with bandwidth DC – 100 MHz, and the secondary voltage v is measured using a N2890A passive voltage probe. In addition to core loss testing, a FLIR Model E60 infrared camera is used to capture the thermal rise during a continuous 30-min excitation.

For strip and small test toroid permeability measurements, we used a Laboratorio Elettrofisico AMH-50 K-S AC/DC hysteresisgraph with a single strip test fixture attachment (Fig. 4). The single strip test fixture consists of a laminated yoke and excitation/measurement coil. The coil contains both primary and secondary windings. From this, the induction field (B) and magnetic field (H) are measured resulting in a permeability value (Eq. 4). Strip test measurements were then compared with the final core measurements by winding the ribbon into a toroid of 31.75-mm OD × 25.4-mm ID with a primary turn count of 38 and secondary turn count of 25. The secondary winding was applied first with the primary winding placed uniformly over the secondary, and the permeability was measured using the hysteresisgraph.

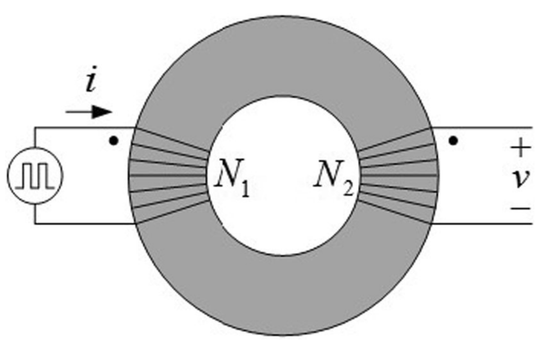

Fig. 3. Conceptual configuration for core loss measurements.

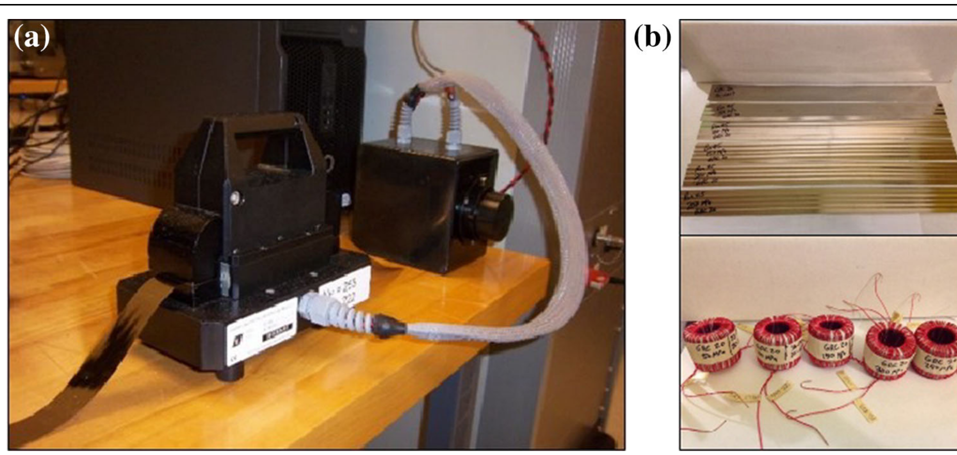

Fig. 4. (a) Single strip test fixture. (b) Strain annealed test ribbons and cores.

Structural Characterization of Ribbons (XRD and TEM)

X-ray diffraction (XRD) was measured in samples of the as-cast and 250-MPa strain annealed ribbon at the Advanced Photon Source Beamline 11-ID-B using a 58.6-keV transmission beam at room temperature. Detector tilt was compensated using a CeO_2 sample, and 1D diffraction patterns were obtained by integrating the intensity from the 2D area detector using FIT2D.[13] Transmission electron microscopy (TEM) and Lorentz imaging were carried out on an FEI Titan G2 80-300 kV TEM. The TEM specimen was prepared following a standard in situ focused-ion beam (FIB) lift-out process such that the sample plane contains the long axis of the ribbon as well as the perpendicular direction normal to the broad ribbon surface. In this way, the ribbon plane contains both an in-plane hard axis along the ribbon length and an easy axis along the perpendicular direction.

MOKE and Lorentz Microscopy Imaging of Domain Structure

An Evico magneto-optical Kerr effect (MOKE) microscope was used to image the domain structure of strain annealed ribbons. Sections of strain annealed ribbon samples were enclosed in a magnetizing coil to produce exciting fields parallel to the ribbon axis. Images were obtained from the "air" side of the ribbon that was not in contact with the wheel during PFC. The ends of the 30-cm-long ribbon samples were connected to the rectangular steel yoke to minimize demagnetizing effects. Images were produced by comparing the remanent state to a reference image captured under an AC excitation.[14] In addition, MOKE images were also acquired from an FIB-sectioned sample prior to thinning to electron transparency for subsequent TEM Lorentz characterization experiments for comparison.

THEORETICAL MODELING

Two-dimensional finite element analysis (2D FEA) was employed to calculate the flux density distribution in the magnetic core of the inductor. When a thin ribbon with varying permeability in the direction of its length is wound to form a core, the permeability will have a gradient in its radial direction. In our FEA model, this is handled by specifying the permeability as a function of radial spatial coordinate.

Consider a case where a ribbon with a thickness t, which includes the effective stacking factor, is wound on a round mandrel of a radius R_i and to an outer radius of R_o. The length of the ribbon l and the stack height (or radial distance from the inner most layer) r are expressed as

$$dl = \frac{2\pi r dr}{t} \tag{5}$$

By integrating this, one finds that

$$l = \frac{\pi}{t}\left(r^2 - R_i^2\right) \tag{6}$$

When the relative permeability changes linearly from μ_i to μ_e over the total length of the ribbon l_e, the relative permeability at length l from the beginning of the winding will be

$$\mu(l) = \frac{\mu_e - \mu_i}{l_e} l + \mu_i \tag{7}$$

Therefore, the relative permeability at a given stack height r will be

$$\mu(r) = \frac{\mu_e - \mu_i}{R_o^2 - R_i^2}\left(r^2 - R_i^2\right) + \mu_i \tag{8}$$

This relationship was used to find the relative permeability at a given position in the wound circular core given an applied tension/permeability versus length profile achieved through strain annealing for subsequent theoretical modeling efforts. The power loss was estimated from the following modified three-term Steinmetz equation:[15]

$$k_{\mathrm{hys}} f B^{\beta} + k_{\mathrm{eddy}} f^2 B^2 + k_{\mathrm{exc}} f^{1.5} B^{1.5} \tag{9}$$

where k_{hys}, k_{eddy}, and k_{exc} are the coefficients for hysteresis, classical eddy current, and excess loss components, respectively. The variable f is the frequency of the current (in kHz), B is the peak flux density (in Tesla), and β is a power constant. This expression was applied to the flux density distribution obtained by FEA. The resultant peak induction, losses, and corresponding temperature distribution were also calculated by 3D FEA for comparison after approximating the radial distribution of the core loss with curve fitting for various assumed permeability profiles throughout the magnetic core. A commercial FEA package, COMSOL Multiphysics, was employed to perform both electromagnetic and thermal FEAs.

EXPERIMENTAL RESULTS

Strain Anneal Processing to Realize Various Ribbon Permeabilities

Using the strain annealing system, a range of tensions was applied as a function of length for a given material speed of 6 cm/s and an annealing temperature of 560°C for a 25-mm-wide, continuous length of ribbon. Figure 5 presents the results of this experiment. The $Co_{74.6}Fe_{2.7}Mn_{2.7}Nb_4Si_2B_{14}$ (at.%) AMR was continuously strain annealed by stepping through a series of tension levels, from 50 MPa to 250 MPa in increments of 50 MPa, with enough material processed at each tension level to wind a small toroid (31.75-mm OD × 25.4-mm ID). In addition, small segments of ribbon (~ 30 cm)

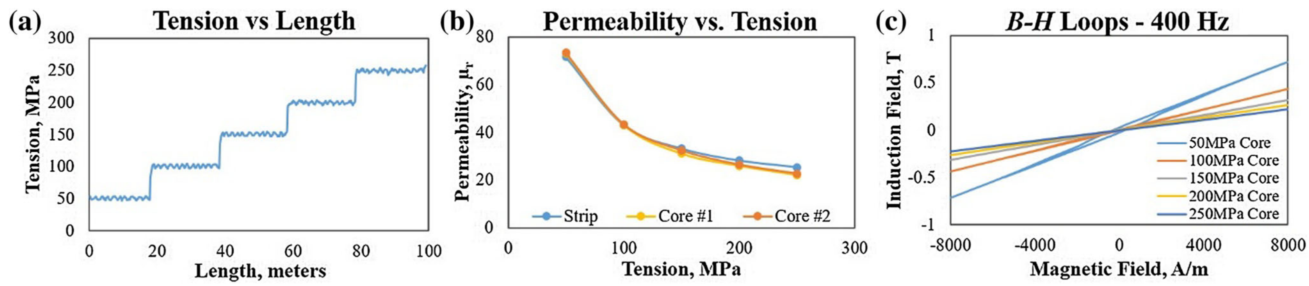

Fig. 5. (a) Tension as a function of length profile, (b) permeability as a function of tension, and (c) *B-H* loops of the targeted applied tensions for the Co-based strips and sample cores (#1 and #2 independent tests) through strain anneal processing.

were cut from the beginning and end of each targeted tension level for quick feedback of strip permeability. As a result, the permeability as a function of the tension relationship was established to enable future processing.

Structural and Magnetic Characterization of Strain Annealed Ribbons

A dark-field transmission electron microscopy (TEM) image is shown in Fig. 6a, which indicates the average grain size of the nanocrystals (bright spots) is less than 10 nm. The corresponding selected area electron diffraction pattern in Fig. 6b suggests a three-phase mixture of fcc and hcp cobalt nanocrystals embedded within an amorphous matrix consistent with the acquired XRD scan presented in Fig. 6d. The broadened rings are due to the fine grain size of the nanocrystals. The EDS spectrum in Fig. 6c shows the material is enriched in Co with lesser amounts of Fe, Mn, Nb, and Si. The Cu signal originated from the Cu TEM grid used to support the sample. The absence of boron in the EDS spectrum is not surprising, as EDS is known to be ineffective in detecting light elements.

Figure 6d compares the transmission XRD patterns of the $Co_{74.6}Fe_{2.7}Mn_{2.7}Nb_4Si_2B_{14}$ ribbon in the as-cast condition with those after strain annealing at 250 MPa. The as-cast condition shows broad peaks confirming the mostly amorphous structure, whereas the strain annealed sample has peak intensities near h–k = 3n using the {hkl} hexagonal indices. The indexed diffraction locations correspond to fcc (a = 3.493 Å) and hcp (a = 2.471 Å and c = 4.035 Å) structures. The broad nature and location of the peaks indicate a high density of planar faults as was reported in similar compositions.[4] Faulting of this type is also present in samples annealed without tension in these alloys.[5]

Figure 7 shows MOKE images of the remanent domain patterns in two samples after strain annealing with 50 MPa and 250 MPa, respectively. The ribbon and applied strain axes are horizontal in the image with Kerr sensitivity aligned parallel to the image vertical. The patterns indicate surface regions with magnetization oriented transverse to the ribbon axis, arranged in bands parallel to the ribbon axis. These configurations minimize demagnetizing fields for bulk domains with significant magnetization components normal to the ribbon plane, similar to those found in grain-oriented Fe-3(wt.%)Si steel under applied tension.[16] The magnetizing field was not sufficient to saturate the material along the ribbon axis given the large K_u, and further work is needed to determine the full domain structure. To complement AMR surface measurements, MOKE imaging was performed for a sample FIB sectioned from the ribbon containing both the strain annealing direction (hard axis) and the direction normal to the broad ribbon surface (easy axis). As expected because of the geometry of the FIB-sectioned sample, a bulk stripe domain structure could be clearly resolved with the domain walls nearly parallel to the easy axis in-plane direction, although some variation was observed, presumably resulting from the demagnetizing field effects due to the shape of the sample.

After subsequent thinning of the FIB lift-out sample to electron transparency, Fig. 8 illustrates the results of Lorentz TEM imaging for comparison demonstrating clear evidence for a stripe domain structure with walls parallel to the in-plane easy axis (normal to the sample edge) and the presence of closure domains near the edge due to local magnetostatic fields.

Prototype Core Fabrication and Testing

Pilot-scale strain annealing using two permeability variations of the $Co_{74.6}Fe_{2.7}Mn_{2.7}Nb_4Si_2B_{14}$ AMR was explored through using the established permeability versus applied tension relationship in Fig. 5-b. Experimental demonstrations of the permeability variations are illustrated in Fig. 9a by applying a uniform tension to obtain a uniform permeability of a tuned value and in Fig. 9b by applying a linearly varying tension with length to achieve a so-called "graded" permeability ribbon. For both the constant and graded tension runs, we produced enough strain annealed ribbon to wind sufficiently sized cores with a targeted permeability of μ = 35. For the ribbon cross section, we used an average ribbon thickness over the entire cast to establish the tension force per unit area (N/mm^2). Ultimately, this method will produce some error in the applied tension force per unit area as the ribbon thickness

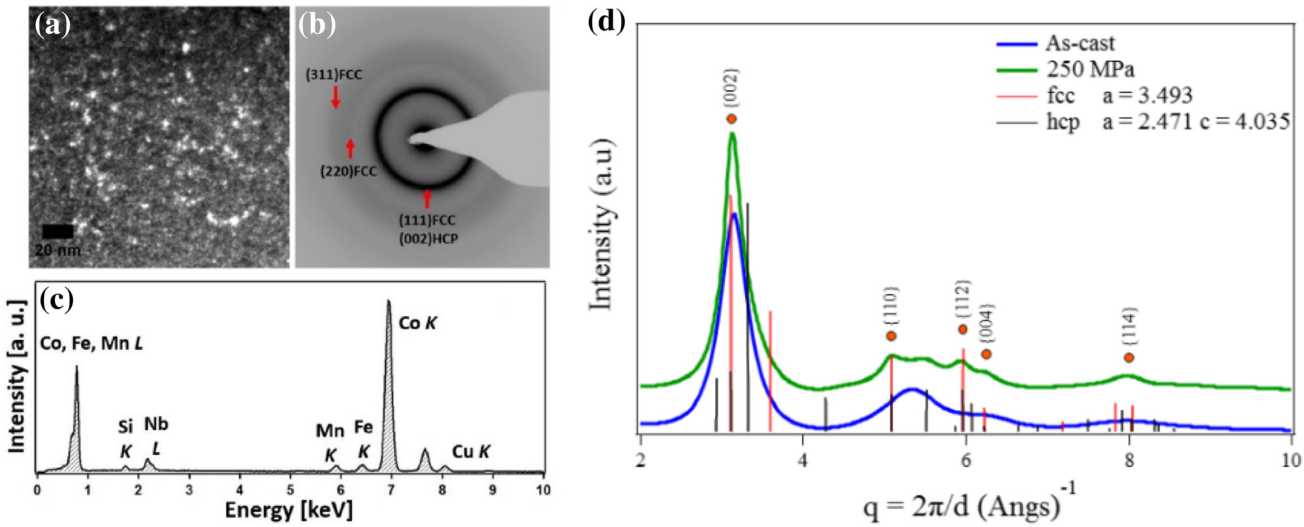

Fig. 6. (a) Dark-field TEM image, (b) corresponding selected area electron diffraction pattern, and (c) EDS spectrum of the material. (d) X-ray diffraction of $Co_{74.6}Fe_{2.7}Mn_{2.7}Nb_4B_{14}Si_2$ ribbon in the amorphous (as-cast) condition and after strain annealing with 250 MPa of tension.

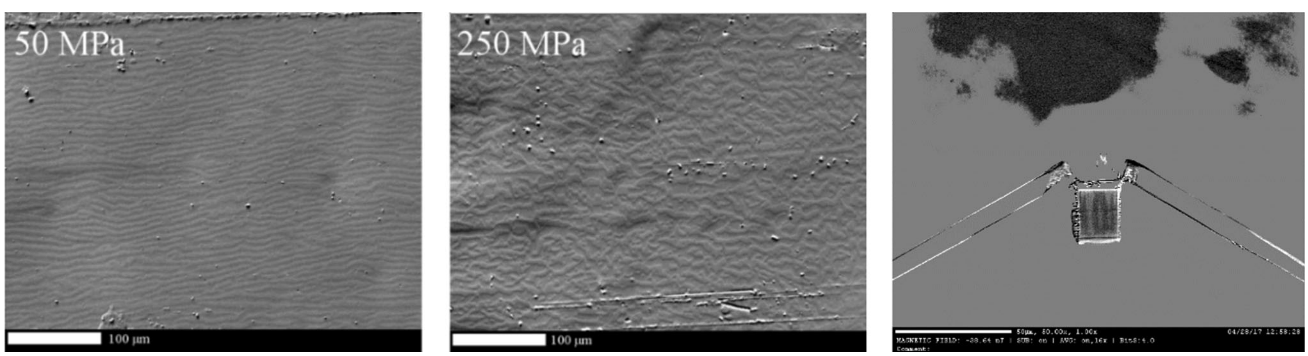

Fig. 7. MOKE image of ribbon samples after strain annealing at 50 (left) and 250 MPa (center) along with a MOKE image obtained from an FIB-sectioned sample (right) containing an easy axis (vertical) and hard axis (horizontal) in the sample plane.

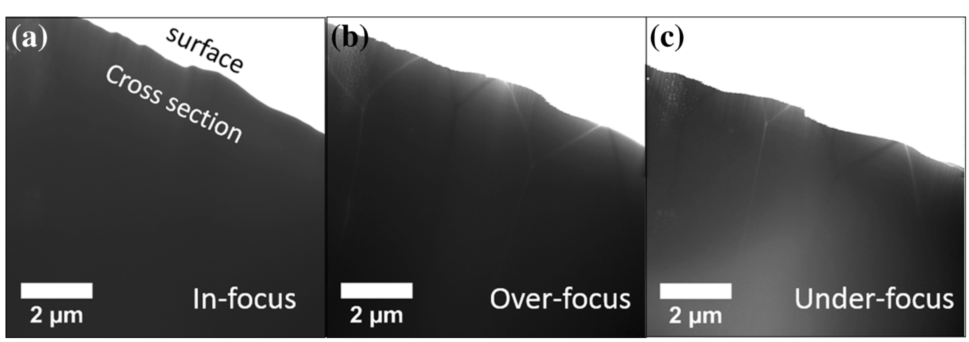

Fig. 8. Lorentz images of the cross section of the ribbon taken at (a) in-focus, (b) over-focus, and (c) under-focus positions. Note the reversal of contrast going from over-focus to under-focus positions confirming domain wall contrast.

during the PFC has some deviation. However, we have found that this accounts for an acceptable ± 4% change in permeability.

To effectively use the permeability as a function of the tension relationship (from Fig. 5b), we used identical processing conditions of the anneal temperature (560°C), material speed (6.1 cm/s), time in the furnace (3.75 s), and rewind tension (15 MPa) to process the constant and graded permeability ribbons. In Table I, tension target values and strip permeabilities are presented for the constant and graded tension ribbons. For the constant tension ribbon, an average annealing tension of 135.7 MPa with a standard deviation of ~ 2 MPa was measured

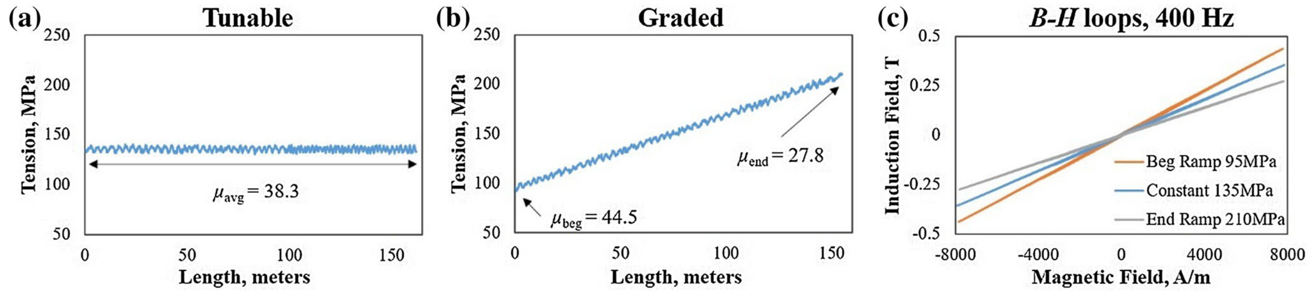

Fig. 9. Experimental examples of two modes of strain annealing to achieve (a) uniform tuned permeability using a constant tension and (b) graded permeability using a constantly varying tension. *B-H* loops comparing the constant tension strip with the beginning and end of the graded tension strip.

Table I. Tension target values and measured strip permeability for constant and graded permeability cores

	Target start tension (MPa)	μ_r (start)	Target end tension (MPa)	μ_r (end)
Constant perm core	135	37.3	135	39.3
Graded perm core	95 (OD)	44.5 (OD)	210 (ID)	27.8 (ID)

during the run. For the graded tension ribbon, a starting annealing tension of 92.3 MPa and finishing tension of 210.7 MPa at a ramp rate of 2.7 MPa/min were measured. It is noted that the strain anneal system controls can ramp the tension with a positive or negative slope, with the chosen graded tension profile requiring fewer rewinding steps.

By winding such strain annealed ribbons (as described in Table I) into a core of selected spatial geometry/dimension, cores with spatially varying permeability profiles can be realized. One major objective of such designs is to produce a more uniform flux distribution present within the core due to the details of the geometrical core shape and winding configuration. As a demonstration of this "flux smoothing" concept, prototype cores were fabricated using the Co-based strain annealed ribbons with constant and graded permeability. For the graded tension core, the winding started with the higher tension, lower permeability ribbon on the inner diameter (ID) ending with the lower tension, higher permeability ribbon on the outer diameter (OD). Examples of the fabricated components (81 mm OD $\times$ 34 mm ID) are presented in Fig. 10.

For each core, the mass was 630 g with an overall stacking factor $\sim$ 70%. Only a small piece of Kapton tape was used to hold together the ribbon ends, and then the cores were placed in an ABS core box with an open end. Furthermore, the windings were layered around the core leaving an unobstructed window of the metal laminated core.

Core Losses and Permeability Measurements

Figure 11 illustrates the custom core loss testing system that was used to excite the constant and graded tension cores during a 30-min continuous test. An H-bridge switching circuit is utilized to apply square voltage waveforms with 50% duty cycles at 20 kHz to the excitation winding. All other experimental setup configurations are given in Table II. The core loss measurements for the two cores were performed under similar B_p values for a fair comparison since the permeability of the constant tension core is larger than the average permeability of the graded tension core, as listed in Table II. Therefore, the amplitudes of the applied square voltages and average excitation currents are manually tuned, in which greater voltage and current amplitudes are utilized with the graded permeability core to compensate the lower average permeability. It is noted that the numbers of primary ($N_1 = 50$) and secondary ($N_2 = 10$) turns are the same for both cores. The average peak flux densities for both cores are $\sim$ 0.15 T, and the average core losses are about 13.1 W and 10.1 W for the constant and graded permeability cores, respectively. The graded permeability core exhibits about 22.6% less core losses (per unit weight) than the constant permeability core at the same flux density condition. Further work is needed to compare cores with identical average permeabilities. In Fig. 12, additional data and details clearly demonstrate a reduction in overall losses at steady state as well as a significant reduction in peak temperature for the graded permeability core as compared with the constant permeability core by approximately 20°C. Linear permeabilities of both the constant and graded permeability core are shown along with stable temperature profiles once steady state is achieved.

At the end of the 30-min continuous test, a thermal image was taken for each core as demonstrated in Fig. 13. It is noted that due to relatively

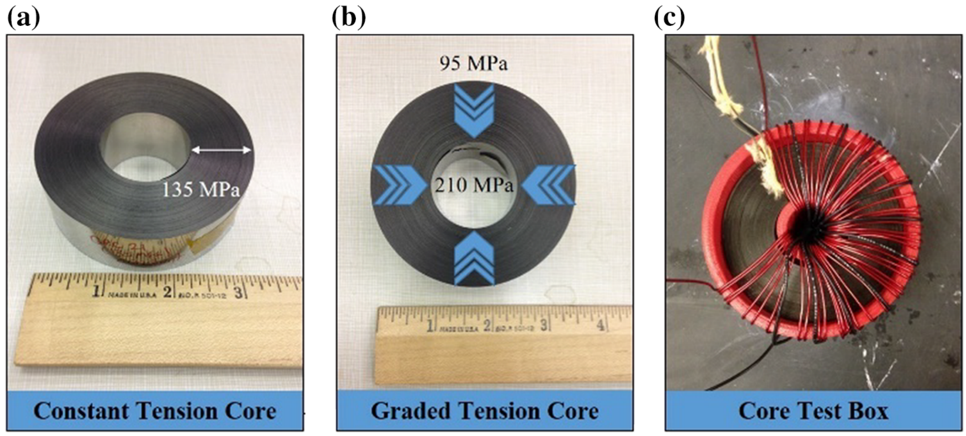

Fig. 10. Photographs of fabricated (a) constant tension and (b) graded permeability cores, along with an (c) ABS core test box and primary (red) and secondary (black) winding profile.

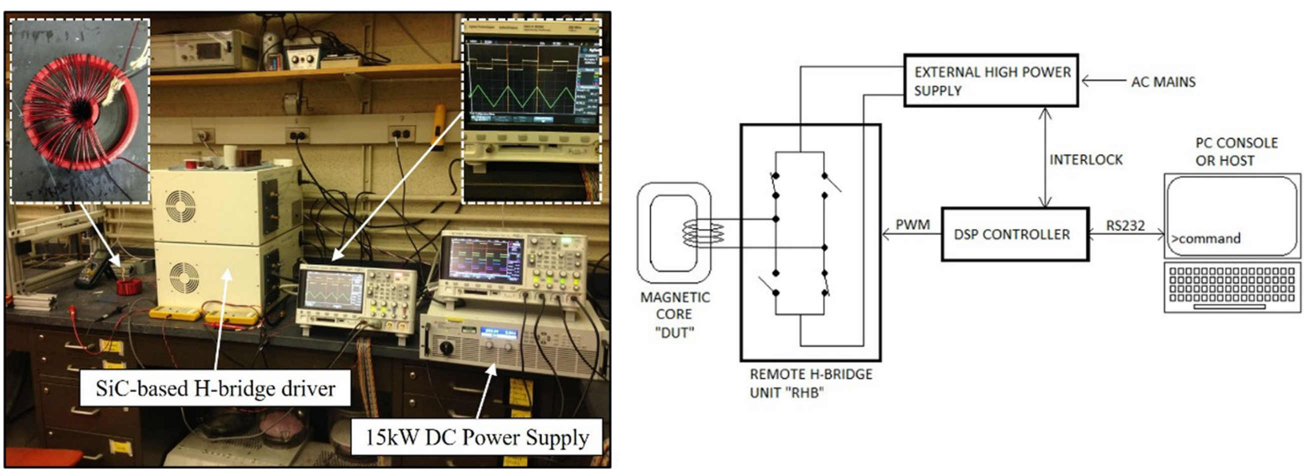

Fig. 11. Custom core loss measurement setup and schematic illustration of the equipment.

Table II. Electrical experiment setup configuration and results

	Constant perm core	Graded perm core
Average peak excitation current i	11.05 A	13.04 A
Average sense voltage, v	55.66 V	66.46 V
Average relative permeability, μ_r	40.0	33.5
Average peak flux density, B_p	0.153 T	0.151 T
Average core loss, P_c	13.11 W	10.15 W
Unit weigh core loss	20.81 W/kg	16.11 W/kg
Loss comparison	100% (base)	77.4%

high primary winding currents, the thermal image was taken immediately after the primary winding's current was switched off to prevent the wire heat from skewing the thermal image. Furthermore, to rule out heating from the wires, we left an exposed section of the core to allow for a clear view of the thermal profile of both the constant (left) and graded (right) permeability cores. Thermal images clearly confirm the impact of the engineered permeability on the peak temperature rise as well as the temperature distribution throughout the core.

MODELING RESULTS

To estimate the theoretically predicted impact of varying permeability spatially throughout a core, 2D FEA was performed as outlined in the

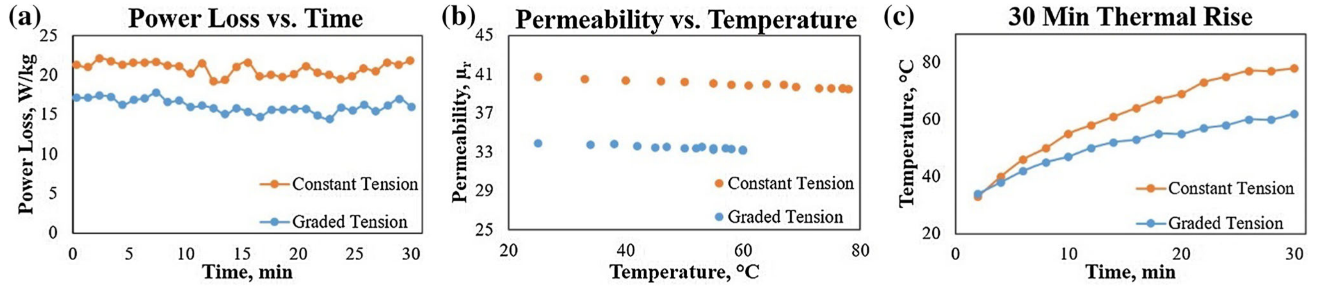

Fig. 12. Using excitation conditions of $f = 20$ kHz and peak induction of $B_p = 0.15$ T, we show (a) close to 25% reduction in power losses, (b) linear permeability as a function of increasing temperature, and (c) time-dependent thermal rise for the constant permeability core as compared with the graded permeability core.

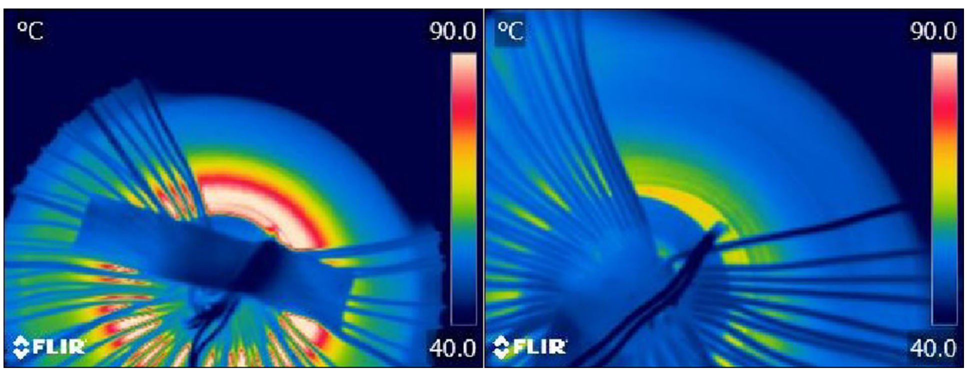

Fig. 13. Experimental thermal imaging at steady state for the constant permeability core (left) compared with the graded permeability core (right).

theoretical procedure section. For the core wound with constant permeability ribbon, a constant value of $\mu = 38.3$ (previously determined from strip testing, Table I) was used for the relative permeability. Similar testing resulted in values of $\mu = 27.8$ for the beginning (ID) and $\mu = 44.5$ for the end (OD) of the graded permeability core. These two values, along with the core geometry, define $\mu(r)$, which gives the permeability at a given point in the core. The density of the core was set to 5.89 kg/l from the mass of the wound core and its geometry. The flux distributions are shown in Fig. 14 at an average flux density of 0.15 T. With the constant permeability core, the flux distribution is highest at the ID where the magnetic path length is shortest and decreases toward the OD. As shown in Fig. 14, this change in the flux density is significantly reduced with the graded core. The relative permeability from the averaged value of the flux density is $\mu = 38.3$ for the constant permeability core and $\mu = 33.0$ for the graded permeability core. These values agree well with the experimental values of $\mu = 40.0$ and $\mu = 33.5$ (Table II) for the constant and graded, respectively.

Because the power loss increases at a higher rate than linear, the constant permeability core shows a higher core loss although the average flux density is set at 0.15 T in both cores (Fig. 15). At 20 kHz, the core loss estimated from the flux density distribution by FEA was 12.2 W for the constant permeability core and 11.2 W for the graded permeability core. The experimental values were 13.11 W and 10.15 W (Table II), respectively, for the constant and graded permeability cores.

The thermal flow is restricted to the radial direction in the wound core because of lower thermal conductivity through laminations. The effective thermal conductivity may only be about one-fifth of that for the in-plane thermal coefficient and is estimated to be about 0.5–1 W/m/K. This creates a sizable temperature gradient along the radius as shown in Fig. 13. A simulated 3D FEA result is shown in Fig. 16. In this calculation, the thermal conductivity of the core was 0.5 W/m/K, and the heat conduction from the core surface was assumed proportional to the temperature difference with the ambient at a rate of 10 W/m^2/K. The simulated results indicate the high temperature region seen in the thermograph for the constant permeability core is caused by the low radial thermal conductivity as well as the presence of the high power loss region near the core's inner radius.

For both the constant and graded permeability cores, the strain annealed material was produced by controlling the permeability profile, described as $\mu(l)$, along the length of the ribbon, l. In the graded permeability core, the permeability profile is approximately linear with ribbon length l. Therefore, the graded permeability core only approximates the balanced flux profile and shows a more

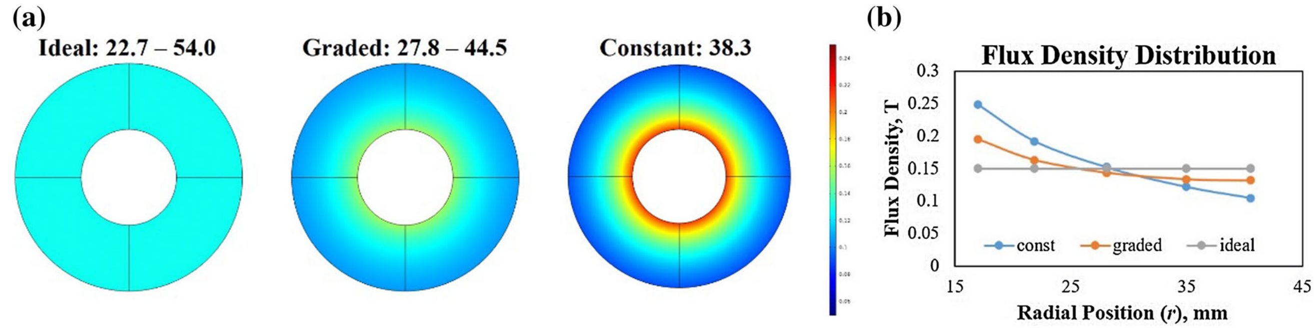

Fig. 14. Flux density distribution comparing the ideally graded, experimentally graded and constant permeability cores using (a) COMSOL simulation modeling and corresponding (b) graphical representation of the flux density as a function of radial position.

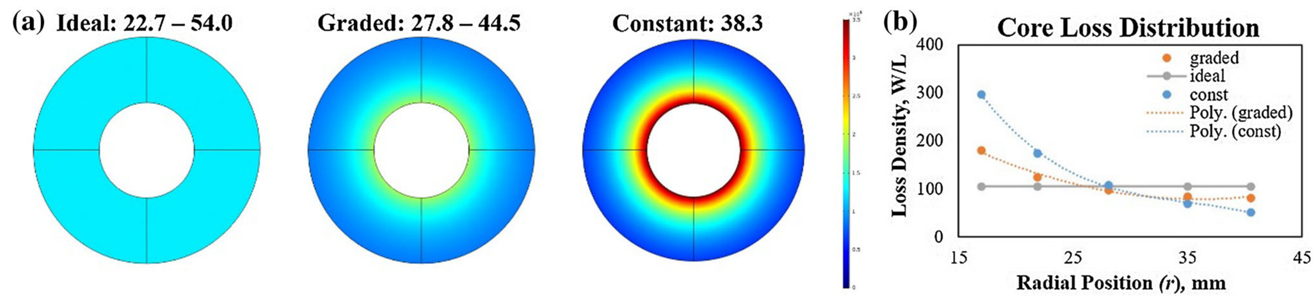

Fig. 15. Core loss distribution comparing the ideally graded, experimentally graded, and constant permeability cores using (a) COMSOL simulation modeling and corresponding (b) graphical representation of power loss density as a function of radial position.

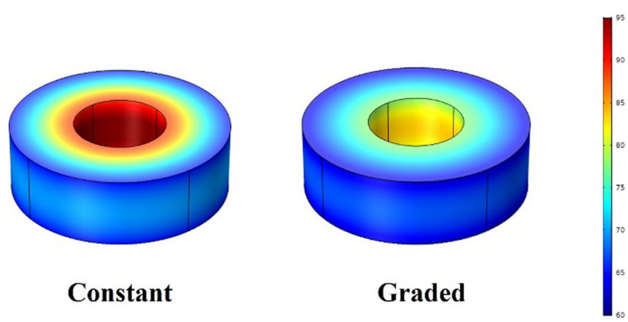

Fig. 16. The 3D FEA thermal profile comparison of the constant and graded permeability cores.

even temperature profile across the core compared with the constant permeability core. However, to fully balance the flux density (as in the ideally graded core), a nonlinear $\mu(l)$ profile is required to produce a linear $\mu(r)$. This nonlinear annealing profile is more important in cores with large values of $(R_o - R_i)/R_i$ with less of an impact when $R_o/R_i \sim 1$, where R_o is the outer radius and R_i is the inner radius.

DISCUSSION AND FORWARD PERSPECTIVE

The ability to create a strain annealed toroid with a specific permeability profile represents a significant advancement for their use in power electronics transformers. Both homogenous and heterogeneous permeabilities can play a role in advanced magnetics design. While transformers generally need a high permeability, some applications such as the flyback transformer[17] or the transformer for series-coupled DC active filters[18] use air gaps to reduce the permeability. The promise of reduced permeability through strain annealing is the elimination of the air gap and all of the associated loss and construction penalties. Another research topic where strain annealing can have a significant impact is in a controlled leakage element. This is most easily realized in axial[19] or tri-axial[20] transformers as shown by Baek.[21] In these designs (as seen in Fig. 17), a core of designed permeability is used to increase and carefully control the effective leakage inductance of the transformer. This is an essential aspect of the design for active bridge power converters.[22] Grading the permeability, as shown, will also improve the leakage core losses and thermal gradient.

Finally, controlled permeability cores can be utilized to tune and control the leakage inductance and leakage flux path of traditional transformers. In Ref. 23, an external limb of the transformer is added to the core to direct flux through a center post. In this approach, it is gapped so as to minimize magnetizing flux. However, a low permeability limb could achieve the same effect without gapping. Similarly, an additional low permeability core is proposed for each winding to augment the leakage inductance and control the flux path in Ref. 24. It is

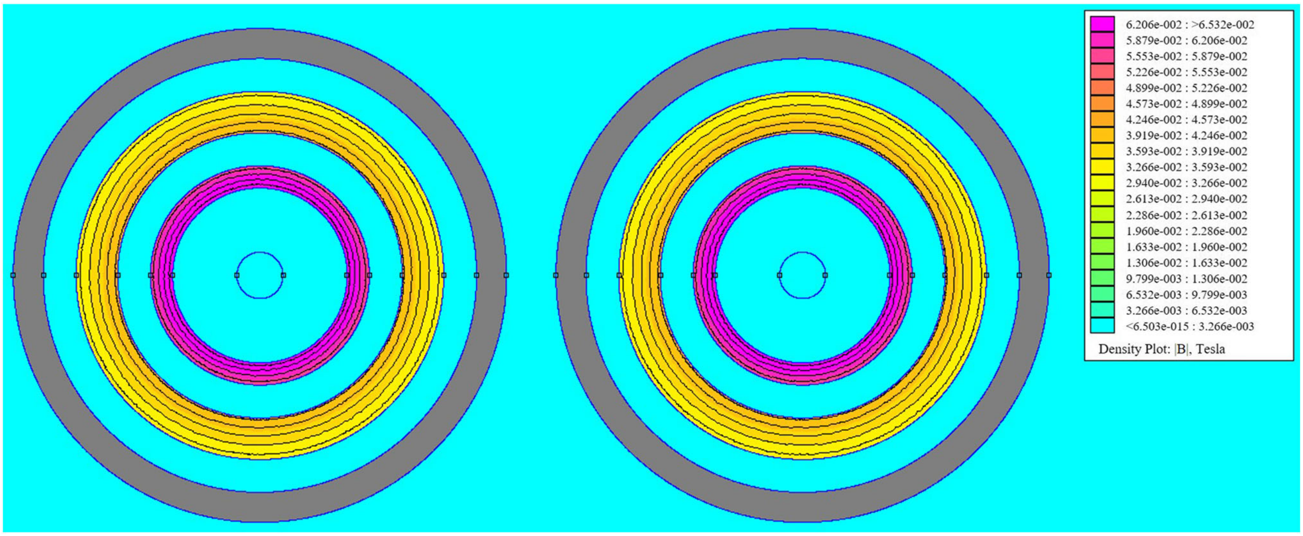

Fig. 17. Tri-axial transformer design with homogenous permeability leakage cores μ = 30 (purple) and μ = 38 (yellow), magnetizing (gray), and windings (blue).

also used as a flux shaping 'shell' to minimize the amount of normal flux entering layers of the magnetic ribbon. The opportunities for applying local permeability engineering to advanced magnetic cores are plentiful, and their applications will only grow as new alloys and advanced strain annealing methods and processes are realized to enable successful application to a broader suite of materials and components.

CONCLUSIONS

MANC alloy cores are prone to many limitations during manufacturing, ranging from simple handling of the material after conventional annealing processes to temperature control during the annealing step due to the exothermic nature of the recrystallization process to furnace and system size for TMF annealing when additional permeability control is needed. By switching to an in-line process, such as strain annealing, we can remove any previously placed constraints set by furnace/system size and therefore remove any restrictions on the core size. However, the successful strain annealing process requires a combination of advanced alloys with optimized mechanical properties, well-characterized responses to applied tension annealing, and soft magnetic properties of interest for advanced magnetic component applications. In this work, we demonstrate the successful realization of spatially varying permeability inductor cores using a monotonically varying applied tension throughout the strain annealing process to accomplish a more uniform flux distribution within the core yielding (1) reduced core losses and (2) a more optimized thermal profile with a reduced peak temperature at the inner core diameter. The selected embodiment of this approach leveraging Co-based nanocomposite alloys for inductor applications is intended to be illustrative of the wealth of opportunities that can be realized through this novel manufacturing approach. Future efforts will target processing of wider width ribbons (50 mm is the widest successfully strain annealed to date) and more advanced permeability profiles such as cyclic permeabilities with sufficiently small spatial periodicities to realize smoothed flux profiles at the corners of racetrack-shaped cores and even more advanced designs to be disclosed in our future works. Cyclic permeabilities have only been realized and have been limited for advanced core fabrication applications in practice because of difficulties in controlling the specific lengths over which permeabilities are averaged over relatively short lengths on the order of $\sim$ centimeters in the presence of applied tensions during the strain annealing process. To fully realize the potential of advanced permeability engineering approaches, new alloys with improved mechanical properties are required as well as enhanced manufacturing processes and procedures.

ACKNOWLEDGEMENTS

The authors acknowledge the support from the DOE Solar Energy Technology Office and the Grid Modernization Laboratory Consortium through the SuNLaMP initiative under Agreement No. DE-EE-00031004. Use of the Advanced Photon Source at Argonne National Laboratory was supported by the U S Department of Energy, Office of Science, Office of Basic Energy Sciences, under Contract No. DE-AC02-06CH11357. The authors also acknowledge P. Zandhuis for all of his contributions in getting the strain annealing system equipped with new control modifications. This technical effort was performed in support of the National Energy Technology Laboratory's ongoing research under the RES Contract DE-FE0004000. This project was funded by the

Department of Energy, National Energy Technology Laboratory, an agency of the United States Government, through a support contract with AECOM. Neither the United States Government nor any agency thereof, nor any of their employees, nor AECOM, nor any of their employees make any warranty, expressed or implied, or assume any legal liability or responsibility for the accuracy, completeness, or usefulness of any information, apparatus, product, or process disclosed, or represent that its use would not infringe privately owned rights. Reference herein to any specific commercial product, process, or service by trade name, trademark, manufacturer, or otherwise does not necessarily constitute or imply its endorsement, recommendation, or favoring by the United States Government or any agency thereof. The views and opinions of authors expressed herein do not necessarily state or reflect those of the United States Government or any agency thereof.

REFERENCES

1. M.E. McHenry and D. E. Laughlin, 19—Magnetic Properties of Metals and Alloys, in *Phys. Metall. (Fifth Edition)*, ed (Oxford: Elsevier, 2014), pp. 1881–2008.
2. M. Willard, Structural and magnetic characterization of HITPERM soft magnetic materials for high temperature applications, Ph.D. Carnegie Mellon University (2000).
3. S. Kernion, P. Ohodnicki, J. Grossmann, A. Leary, S. Shen, V. Keylin, J. Huth, J. Horwath, M. Lucas, and M.E. McHenry, *Appl. Phys. Lett.* 101, 102408 (2012).
4. A. Leary, V. Keylin, A. Devaraj, V. DeGeorge, P. Ohodnicki, and M.E. McHenry, *J. Mater. Res.* 31, 3089 (2016).
5. A. Leary, V. Keylin, P. Ohodnicki, and M.E. McHenry, *J. Appl. Phys.* 117, 17A338 (2015).
6. N. Aronhime, V. Degeorge, V. Keylin, P.R. Ohodnicki, and M. McHenry, *JOM* 69, 2164 (2017).
7. G. Herzer, V. Budinsky, and C. Polak, *J. Phys. Conf. Ser.* 266, 557 (2011).
8. P.R. Ohodnicki, Y.L. Qin, D.E. Laughlin, M.E. McHenry, M. Kodzuka, T. Ohkubo, K. Hono, and M.A. Willard, *Acta Mater.* 57, 87 (2009).
9. P.R. Ohodnicki, D.E. Laughlin, M.E. McHenry, V. Keylin, and J. Huth, *J. Appl. Phys.* 105, 07A322 (2009).
10. P.R. Ohodnicki, J. Long, D.E. Laughlin, M.E. McHenry, V. Keylin, and J. Huth, *J. Appl. Phys.* 104, 113909 (2008).
11. J. Kapoor and C. Polak, Soft magnetic core with position-dependent permeability, US20150070124 A1 (2015).
12. J. Muhlethaler, J. Biela, J.W. Kolar, and A. Ecklebe, *IEEE Trans. Power Electron.* 27, 953 (2012).
13. A.P. Hammersley, *ESRF Internal Report,* ESRF97HA02T, FIT2D: An Introduction and Overview (1997).
14. I.V. Soldatov and R. Schäfer, *Rev. Sci. Instrum.* 88, 073701 (2017).
15. C.P. Steinmetz, *Trans. Am. Inst. Electr. Eng.* IX, 1 (1892).
16. O. Perevertov, J. Thielsch, and R. Schäfer, *J. Magn. Magn. Mater.* 385, 358 (2015).
17. R.W. Erickson and D. Maksimovic, *Fundamentals of Power Electronics* (Berlin: Springer, 2001).
18. R. Beddingfield, A. Davis, H. Mirzaee, and S. Bhattacharya, Investigation of series DC active filter and hybrid AC active filter performance in medium voltage DC amplfier, in *2015 IEEE Electric Ship Technologies Symposium (ESTS)* (2015), pp. 161–166.
19. K.W. Klontz, Analysis and Design of a Coaxial Winding Transformer Interface for an Electric Vehicle Charging System, Ph.D. University of Wisconsin-Madison (1995).
20. H.L.N. Wiegman, A DC/DC Converter for a Dual Voltage Automotive System, M.S. University of Wisconsin-Madison (1991).
21. S. Baek, High-frequency AC-link for Medium-Voltage DC/DC Converters and Solid State Transformer Applications, Ph.D. North Carolina State University (2014).
22. M.H. Kheraluwala, High-power high-frequency dc-to-dc converters, Ph.D. University of Wisconsin-Madison (1991).
23. J. Muhlethaler, J. Biela, J.W. Kolar, and A. Ecklebe, *IEEE Trans. Power Electron.* 27, 964 (2012).
24. R. Beddingfield, S. Bhatacharya, P. Ohodnicki, and K. Byerly, Mixed Material Magnetic Core for Shielding of Eddy Current Induced Excess Losses, United States of America Provisional Patent 221404-8470, 62/582,107 (2017).